Received: 23 March 2024 | Accepted: 15 June 2024

DOI: 10.1002/ame2.12468

ORIGINAL ARTICLE

Endogenous Fe^{2+}-triggered self-targeting nanomicelles for self-amplifying intracellular oxidative stress

Zhongxiong Fan[1] | Guoyu Xia[1] | Qingluo Wang[1] | Shiduan Chen[2] | Jianmin Li[1] | Zhenqing Hou[1,2] | Ziwen Jiang[3] | Juan Feng[4]

[1]School of Pharmaceutical Sciences and Institute of Materia Medica, Xinjiang University, Urumqi, China

[2]College of Materials, Xiamen University, Xiamen, China

[3]Department of Gynecology, Beijing Obstetrics and Gynecology Hospital, Capital Medical University, Beijing Maternal and Child Health Care Hospital, Beijing, China

[4]Department of Hematology, The First Affiliated Hospital of Xiamen University and Institute of Hematology, School of Medicine, Xiamen University, Xiamen, China

Correspondence
Zhongxiong Fan, School of Pharmaceutical Sciences and Institute of Materia Medica, Xinjiang University, Urumqi 830017, China.
Email: fanzhongxiong@xju.edu.cn

Ziwen Jiang, Department of Gynecology, Beijing Obstetrics and Gynecology Hospital, Capital Medical University, Beijing Maternal and Child Health Care Hospital, Beijing 100006, China.
Email: jiangziwen@ccmu.edu.cn

Juan Feng, Department of Hematology, The First Affiliated Hospital of Xiamen University and Institute of Hematology, School of Medicine, Xiamen University, Xiamen, 361003, China.
Email: fengjuannihao@163.com

Funding information
National Natural Science Foundation of China, Grant/Award Number: 82000152; Natural Science Foundation of Xinjiang Uygur Autonomous Region, Grant/Award Number: 2022D01C698; Xinjiang Uygur Autonomous Region Tianchi Talent Introduction Program-Young Doctor, Grant/Award Number: 51052300514; Key research and development program in Xinjiang Uygur Autonomous Region, Grant/Award Number: 2023B02030 and 2023B02030-1; Autonomous Region universities basic research funds research projects-cultivation projects, Grant/Award Number: XJEDU2023P017

Abstract

Background: Artesunate (ASA) acts as an $\bullet O_2^-$ source through the breakdown of endoperoxide bridges catalyzed by Fe^{2+}, yet its efficacy in ASA-based nanodrugs is limited by poor intracellular delivery.

Methods: ASA–hyaluronic acid (HA) conjugates were formed from hydrophobic ASA and hydrophilic HA by an esterification reaction first, and then self-targeting nanomicelles (NM) were developed using the fact that the amphiphilic conjugates of ASA and HA are capable of self-assembling in aqueous environments.

Results: These ASA–HA NMs utilize CD44 receptor-mediated transcytosis to greatly enhance uptake by breast cancer cells. Subsequently, endogenous Fe^{2+} from the tumor catalyzes the released ASA to produce highly toxic $\bullet O_2^-$ radicals to kill tumor cells, although sustained tumor growth inhibition can be achieved via in vivo experiments.

Conclusions: Self-targeting NMs represent a promising strategy for enhancing ASA-based treatments, leveraging clinically approved drugs to expedite drug development and clinical research in oncology.

KEYWORDS
nanomicelles, non-Fenton, oxidative stress, reactive oxygen species, self-targeting

Zhongxiong Fan, Guoyu Xia, and Qingluo Wang have contributed equally to this work.

1 | INTRODUCTION

Very recently, reactive oxygen species (ROS)–dominated oxidative stress has become an effective antitumor strategy.[1] Three ROS-dominated oncotherapies, namely photodynamic therapy (PDT), sonodynamic therapy (SDT), and radiotherapy (RT), can produce ROS for enhancing oxidative stress in tumor cells.[1,2] However, these techniques face challenges such as the poor tissue penetration ability of lasers in PDT,[3] the low quantum yield of the sonosensitizer in SDT,[4] and the inherent toxicity toward normal cells in RT.[5] In addition, the introduction of exogenous equipment such as laser device, ultrasonic probe, and X-ray source seriously hinders further application of PDT, SDT, and RT, respectively.[6,7] To eliminate the need for external equipment, chemodynamic therapy (CDT) utilizes Fenton/Fenton-like reactions to produce toxic ROS against tumor cells, presenting a hopeful anticancer approach. Nevertheless, the restricted H_2O_2 concentration (~50–100 μm) and mild acidity (pH 6.5) in the tumor microenvironment compromise the efficacy of Fenton/Fenton-like reactions, thereby resulting in low ROS production.[6,8] This phenomenon may occur due to the fact that the effectiveness of the Fenton/Fenton-like reaction is guaranteed only under relatively high levels of H_2O_2 and low pH values (2–4).[9,10] Therefore, to effectively overcome these disadvantages of CDT based on Fenton/Fenton-like reaction, this concept of the non-Fenton CDT without the high-abundance H_2O_2 and low pH value (2–4) requirements has been proposed by our group.[11] For example, we fixed our focus on the antimalarial drug artesunate (ASA). It is worth noting that substantial evidence suggests that ASA can exhibit antitumor activity through various mechanisms, such as inhibiting tumor cell proliferation, blocking the cell cycle, and inducing oxidative stress,[12] which can be attributed to the well-established theory that tumor endogenous Fe^{2+} can catalyze the peroxo-bridge bond in ASA, resulting in the production of highly toxic $\bullet O_2^-$ radicals.[13] However, the efficacy of ASA is seriously weakened by some inherent disadvantages such as high hydrophobicity, poor pharmacokinetics, and low bioavailability.[14,15] To address these disadvantages, one efficient strategy is to encapsulate ASA into various nanocarriers to obtain ASA-based nanodrugs.[16] Even so, the lack of self-targeting tumor effect still hinders the further application of ASA-based nanodrugs in oncotherapy. Therefore, how to endow ASA-based nanodrugs with self-targeting tumor effect is crucial in non-Fenton CDT of ASA.

Well known for their effectiveness, self-targeting nanodrugs can significantly improve the targeted accumulation of nanodrugs within the tumor region, thereby minimizing adverse effects on healthy cells or organs.[17] Notably, although some exogenous targeting ligands such as folic acid, hyaluronic acid (HA), antibodies, and peptides exhibit binding affinity to receptors overexpressed on the surface of tumor cell membranes, these exogenous ligands themselves have minimal therapeutic effects and serve only as targeting ligands for the specific delivery of nanodrugs.[18] A careful comparison of the aforementioned ligands shows that HA has an excellent water solubility, biocompatibility, and biodegradability.[19] In addition, HA can be directly regarded as a drug carrier, which can specifically bind to the CD44 receptor on the surface of the tumor cells and facilitate drug delivery.[20] Therefore, how to modify these exogenous ligands and include HA in some multifunctional molecules with therapeutic and self-targeting effect are beneficial for simplifying the preparation process and internal structure of self-targeting nanodrugs, thereby providing some possibilities for the clinical application of self-targeting nanodrugs.

With regard to the aforementioned factors, as shown in Scheme 1, both hydrophilic HA and hydrophobic ASA are conjugated by a hydrolyzable ester bond to synthesize the amphiphilic ASA–HA conjugate. The amphiphilicity of the ASA–HA conjugate enables direct self-assembly into endogenous Fe^{2+}-triggered self-targeting ASA–HA nanomicelles (NM). The benefit of ASA–HA NMs lies in their ability to specifically transport non-Fenton antitumor CDT agents into tumor cells in vivo via a self-targeting effect mediated by CD44 receptors. By facilitating the self-amplification of oxidative stress within tumor cells, HA added to ASA–HA NMs effectively reduces phagocytosis by macrophages while circulating in the body. This feature helps minimize potential side effects on healthy cells or organs.[21] On reaching the tumor region, the HA ligands will autonomously target the CD44 receptors on the surface of tumor cells, thereby improving the accumulation within the tumor and enhancing the cellular uptake of ASA–HA NMs.[22] In addition,

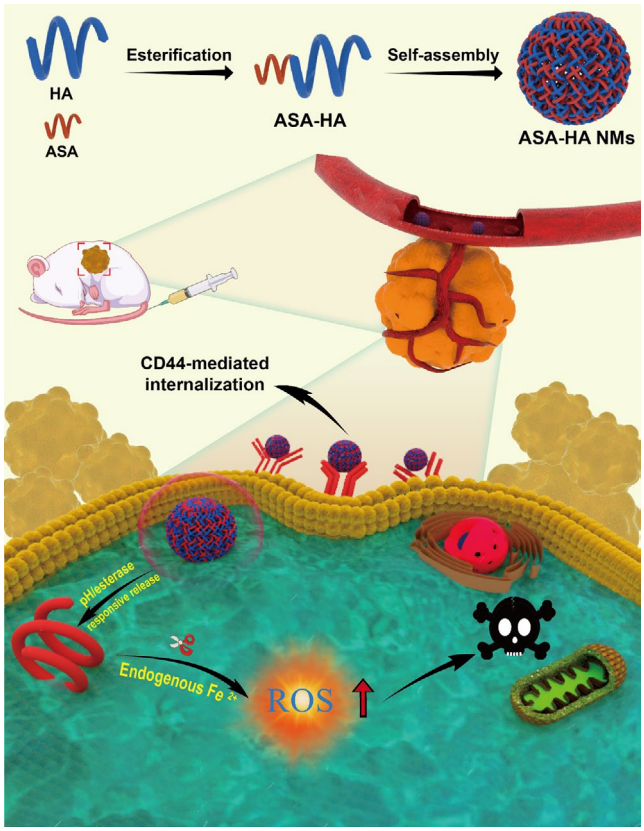

SCHEME 1 Schematic illustration of endogenous Fe^{2+}-triggered self-targeting ASA–HA (artesunate–hyaluronic acid) NMs (nanomicelles) for self-amplifying intracellular oxidative stress.

the acidic esterase-rich lysosome from tumor cells will result in the rapid liberation of ASA within tumor cells. Subsequently, the liberated ASA undergoes catalysis by endogenous Fe^{2+} in tumor cells to produce a potent $\bullet O_2^-$ surge, fostering self-amplifying intracellular oxidative stress. In brief, we propose a new orientation for oxidative stress-mediated self-targeting oncotherapy.

2 | MATERIALS AND METHODS

2.1 | Materials

ASA, 4-dimethylaminopyridine (DMAP), 1-(3-dimethylaminopropyl)-3-ethylcarbodiimide (EDC), and Hoechst 33258 were obtained from Shanghai Myriad Chemical Technology Co. HA was obtained from Chengdu McCarthy Chemical Co., Ltd. Disodium hydrogen phosphate, paraformaldehyde, fetal bovine serum (FBS-ST30-3302), isoflurane, and 4-chloro-7-nitro-1,2,3-benzoxadiazole (NBD-Cl) were purchased from Shanghai Maclean Biochemical Technology Co., Ltd. Cyanine 5.5 (Cy5.5) was obtained from Xi'an Ruixi Biotechnology Co., Ltd (Xi'an, China). Unless specified otherwise, all chemical reagents were of analytical grade and commercially available, and used without further purification. Experiments were conducted following relevant laws and institutional guidelines. Animal experiments adhered to the guidelines set by the Ethical Committee of Xiamen University.

2.2 | Synthesis and characterization of ASA–HA conjugate

The amphiphilic ASA–HA conjugate was synthesized through an esterification reaction between hydrophobic ASA and hydrophilic HA. Initially, 57.6 mg of ASA (0.15 mmol) was weighed and dissolved in 3 mL of dimethyl sulfoxide (DMSO). Subsequently, 76 mg of EDC (0.40 mmol) and 45 mg of DMAP (0.37 mmol) were added to the solution; the mixture was stored in a dark environment and stirred at room temperature for 1 h to activate the carboxyl group. After the carboxyl group of ASA was activated, 50 mg of HA was dissolved in 3 mL of formamide; and the mixture was added to the ASA solution. Subsequently, the reaction mixture was stirred on a heated magnetic stirrer at 50°C for 12 h under dark conditions and stirred again at room temperature for 36 h to ensure complete progress of the esterification reaction. Throughout the entire reaction, the solution was shielded with nitrogen. Subsequently, the solution was carefully transferred into a dialysis bag with a molecular weight cut-off (MWCO) of 3500 Da (Slide-A-Lyzer, Thermo Scientific, USA) and dialyzed using a mixture of deionized (DI) water and EtOH in varying ratios (1:3, 1:2, and 1:1) for 8 h each to facilitate the purification process. Finally, the dialysis was continued with DI water for an additional 24 h to remove any remaining DMAP, EDC, and organic solvents. The resulting product was then filtered through an aqueous filter membrane and dried under vacuum to obtain the final product.

Next, to characterize the ASA–HA conjugate, Fourier-transform infrared (FT-IR) spectrum analysis was performed using a Nicolet IS50 infrared spectrometer (Thermo Fisher, USA). The UV–Vis. absorption spectra were obtained using a UV–Vis. spectrophotometer UV2550 (Shimadzu, Japan). The proton nuclear magnetic resonance (^{1}H-NMR) spectra were analyzed using a Bruker AVANCE III HD 300 MHz NMR spectrometer (Bruker, Germany) using the solution of both DMSO-d_6 and D_2O as solvents. The X-ray diffraction (XRD) pattern was tested using an XRD analyzer D8-A25 (Bruker). In addition, ASA, HA, and ASA + HA (the physical mixture of ASA and HA) were used as control groups in the aforementioned characterization.

2.3 | Synthesis and characterization of ASA–HA NMs

ASA–HA NMs were synthesized using a cosolvent method, according to our previous report.[23] In brief, 10 mg of the already-synthesized ASA–HA conjugate was dispersed in 0.5 mL of DMSO and placed in an ultrasonic cleaner (200 W) for ~0.5 h in an ice-water bath. The resulting DMSO solution was slowly added dropwise to 4.5 mL of preprepared DI water to obtain a 2-mg/mL dispersion of the ASA–HA conjugate. This mixture was then shaken in a constant temperature shaker (37°C, 100 rpm) for 3 h under lightproof conditions to produce ASA–HA NM dispersion. The obtained ASA–HA NM dispersion was transferred to a dialysis bag (MWCO = 3500 Da) and then dialyzed using a DI water–EtOH (v:v, 1:3, 1:2, and 1:1) solution for 8 h based on each proportion. Then, dialysis was continued using DI water to further remove the unassembled ASA–HA conjugate and trace organic solvents for 24 h. Finally, to obtain the ASA–HA NMs of uniform hydrodynamic size and good dispersion, the obtained ASA–HA NMs were further extruded using aqueous microporous filter membranes (Millex needle filter, pore size: 220 nm; diameter: 33 mm, sterility, hydrophilicity, USA).

Next, to characterize the ASA–HA NMs, a Malvern Zetasizer 2000 (Malvern, UK) was utilized. This instrument was used to measure the hydrodynamic particle size and surface potential of the ASA–HA NMs using dynamic light scattering (DLS) and electrophoretic light scattering (ELS), respectively. The morphology of the ASA–HA NMs was visualized using a transmission electron microscope (JEM2100, JEOL, Tokyo, Japan). Drug payload of ASA–HA NMs was quantified using a UV–Vis. spectrophotometer UV2550 (Shimadzu).

2.4 | Determination of critical micelle concentration value

Critical micelle concentration (CMC) value for the ASA–HA conjugate was assessed using fluorescence probes. The associated experimental procedures are as follows: acetone solution of pyrene (5×10^{-5} M) was added to each test tube, and acetone was allowed to evaporate and dry naturally. Then, 1 mg/mL of ASA–HA NMs in

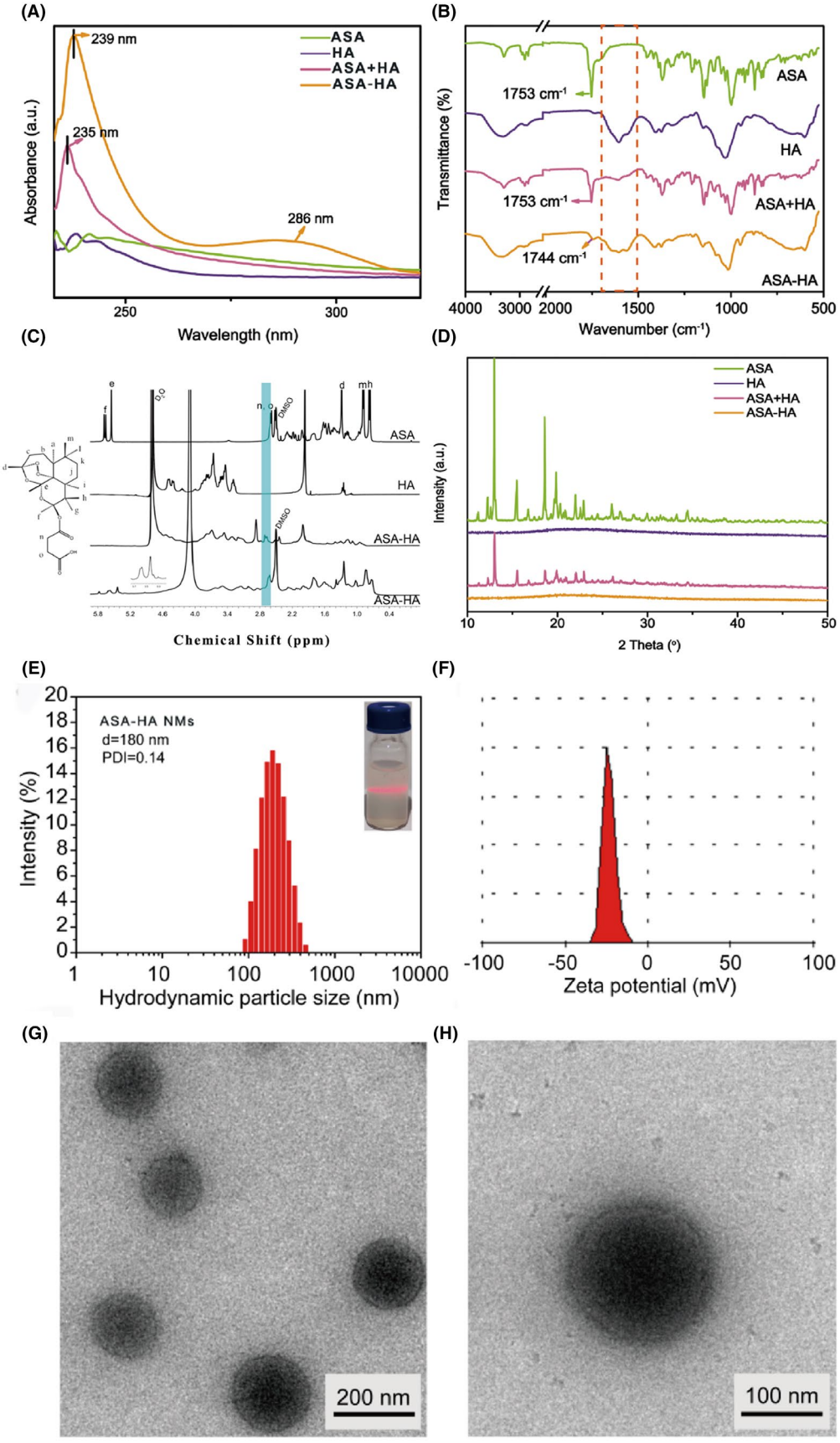
(A)
239 nm
235 nm
286 nm
ASA
HA
ASA+HA
ASA-HA
Absorbance (a.u.)
Wavelength (nm)
(B)
1753 cm-1
1753 cm-1
1744 cm-1
ASA
HA
ASA+HA
ASA-HA
Transmittance (%)
Wavenumber (cm-1)
(C)
ASA
HA
ASA-HA
ASA-HA
DMSO
Chemical Shift (ppm)
(D)
ASA
HA
ASA+HA
ASA-HA
Intensity (a.u.)
2 Theta (°)
(E)
ASA-HA NMs
d=180 nm
PDI=0.14
Intensity (%)
Hydrodynamic particle size (nm)
(F)
Zeta potential (mV)
(G)
200 nm
(H)
100 nm

FIGURE 1 Characterization of ASA–HA (artesunate–hyaluronic acid) conjugate and ASA–HA NMs (nanomicelles). (A) UV–Vis. and (B) FT-IR (Fourier-transform infrared) spectra of ASA, HA, ASA + HA, and ASA–HA conjugate. (C) ^{1}H-NMR of ASA (the solvent was DMSO-d_6), HA (the solvent was D_2O), and ASA–HA conjugate (the solvent was the solution of DMSO and D_2O, and the ratio of DMSO to D_2O was 2:1). (D) XRD (X-ray diffraction) spectra of ASA, HA, ASA + HA, and ASA–HA conjugate. (E) Hydrodynamic particle size (insert: Tyndall effect), (F) zeta potential, (G) transmission electron microscopic image, and (H) enlarged transmission electron microscopic images of ASA–HA NMs.

phosphate-buffered saline (PBS) was diluted to a series of concentrations and added to these tubes. Each tube contained 3 mL of solution at pH 7.4. All samples were sonicated in an ice-water bath for 0.5 h, incubated at 40°C for an additional 0.5 h, and then left overnight at 60°C. Finally, the fluorescence intensity of all samples was measured using a Hitachi F4500 fluorescence spectrophotometer (Hitachi, Japan).

2.5 | Drug release of ASA–HA NMs

In vitro release behaviors of ASA in ASA–HA NMs were evaluated using a series of simulated physiological conditions. In brief, 3 mL of pure ASA drug or ASA–HA NM solution (with an ASA concentration of 1 mg/mL) was placed in a dialysis bag (MWCO = 3500 Da, Slide-A-Lyzer, Thermo Scientific), and the bag was placed in a beaker containing 17 mL of PBS (pH 7.4, 6.5, or 5.0) with/without esterase (5 mg, 30 U/mL). Then, 3 mL of external PBS was removed and promptly replaced with 3 mL of fresh PBS at predetermined time intervals. The released amount of ASA was determined using the UV–Vis. spectrophotometer UV2550 (Shimadzu). Finally, the cumulative release of ASA was calculated using the following equation:

$$\text{Cumulative release}(\%) = \frac{3 \times \sum_{i=1}^{n-1} Ci + 20 \times Cn}{\text{weight of drug in the ASA} - \text{HA NMs}} \times 100\%$$

Where, n: the number of dialysate collection time points; Ci: Drug concentration in the dialysate at time point (n-1); Cn: Drug concentration in the dialysate at time point (n).

2.6 | Cell line

The cell lines utilized were sourced from the American Type Culture Collection. HeLa (human cervical cancer cells) and A549 cells (human lung cancer cells) were cultured in Dulbecco's modified Eagle's medium, whereas 4T1 (mouse breast cancer cells) and L02 cells (human normal hepatocytes) were cultured in RPMI 1640.

2.7 | In vitro cellular uptake

To assess the cellular uptake in vitro of ASA–HA NMs, ASA and ASA–HA were tagged with NBD-Cl, a small molecular structure, through a nucleophilic substitution reaction (termed as ASA^{NBD} and ASA^{NBD}–HA NMs), according to our previous report.[24] HeLa cells known for their high expression of CD44 receptors, A549 cells with a low expression of CD44 receptors, and L02 cells lacking CD44 receptor expression were seeded into six-well plates and then treated with ASA^{NBD} and ASA^{NBD}–HA NMs based on 75 μg/mL of NBD concentration for 1 and 4 h. Finally, the cellular uptake effect of ASA–HA NMs was qualitatively analyzed using a confocal laser scanning microscope (Leica TCS SP5, Germany).

Further, flow cytometry analysis was used to quantitatively determine the cellular uptake of ASA–HA NMs. HeLa, A549, and L02 cells were seeded into six-well plates and then treated with ASA^{NBD} and ASA^{NBD}–HA NMs based on 75 μg/mL of NBD for 1 and 4 h, respectively. The cellular fluorescence intensity of NBD was captured using a FACSCalibur flow cytometer (Becton Dickinson, USA), and the results were analyzed using Cell Quest software.

2.8 | In vitro cytotoxicity

MTT assay was conducted to evaluate the in vitro cytotoxic effect of ASA, ASA + HA physical mixture, and ASA–HA NMs on HeLa, A549, and L02 cells. In brief, HeLa, A549, and L02 cells were seeded in 96-well plates and incubated for 24 h. Cell viability was assessed using the 3-(4,5-dimethylthiazol-2-yl)-2,5-diphenyltetrazolium bromide (MTT) assay following the manufacturer's instructions. The absorbance values were measured using an ELISA reader (WD-2102B, Beijing, China). Subsequently, the half-maximal inhibitory concentrations (IC50) in cells were calculated using SPSS Statistics 20.0 software.

Next, the apoptosis effect of ASA–HA NMs was also determined using the Annexin V-FITC/PI Apoptosis Detection Kit (BD Biosciences, USA). In detail, HeLa cells (5.0×10^5 cells/well) were seeded in six-well plates. After incubation for 24 h, the cells were separately incubated with PBS (control), ASA, ASA + HA, and ASA–HA NMs at ASA of 75 μg/mL. Finally, the cells were analyzed using a FACSCalibur flow cytometer (Becton Dickinson), and the results were analyzed utilizing Cell Quest software.

2.9 | Intracellular ROS determination

The intracellular production of ROS in HeLa cells was assessed using 2,7-Dichlorodihydrofluorescein diacetate (DCFH-DA). Initially, HeLa cells were seeded in six-well plates. Subsequently, the cell culture was removed, and the cells were washed thrice with PBS. The HeLa cells were then incubated with ASA and ASA–HA NMs at a concentration of 75 μg/mL of ASA for 1 and 4 h, respectively. Then, the cell nuclei were stained with Hoechst 33258 for 10 min. Finally, the

effect of ROS production was assessed using a confocal laser scanning microscope (Leica TCS SP5).

2.10 | Animals

Female Kunming mice (aged 4–6 weeks and weighing 20–22 g) were obtained from the Xiamen University Laboratory Animal Center. All animal experiments were performed in compliance with the guidelines and policies of the Animal Care and Use Committee of Xiamen University. The Kunming mice were subcutaneously injected with 4T1 cells expressing high levels of CD44 receptors in the right hind limb to develop a tumor model.

2.11 | In vivo fluorescence imaging

To assess the self-targeting effect of ASA–HA NMs, in vivo fluorescence imaging of the tumor-bearing mice was conducted. Briefly, ASA and ASA–HA were conjugated using a near-infrared fluorescence probe Cy5.5-NH2 through an amide reaction (named as $ASA^{Cy5.5}$ and $ASA^{Cy5.5}$–HA NMs), according to our previous report.[23]

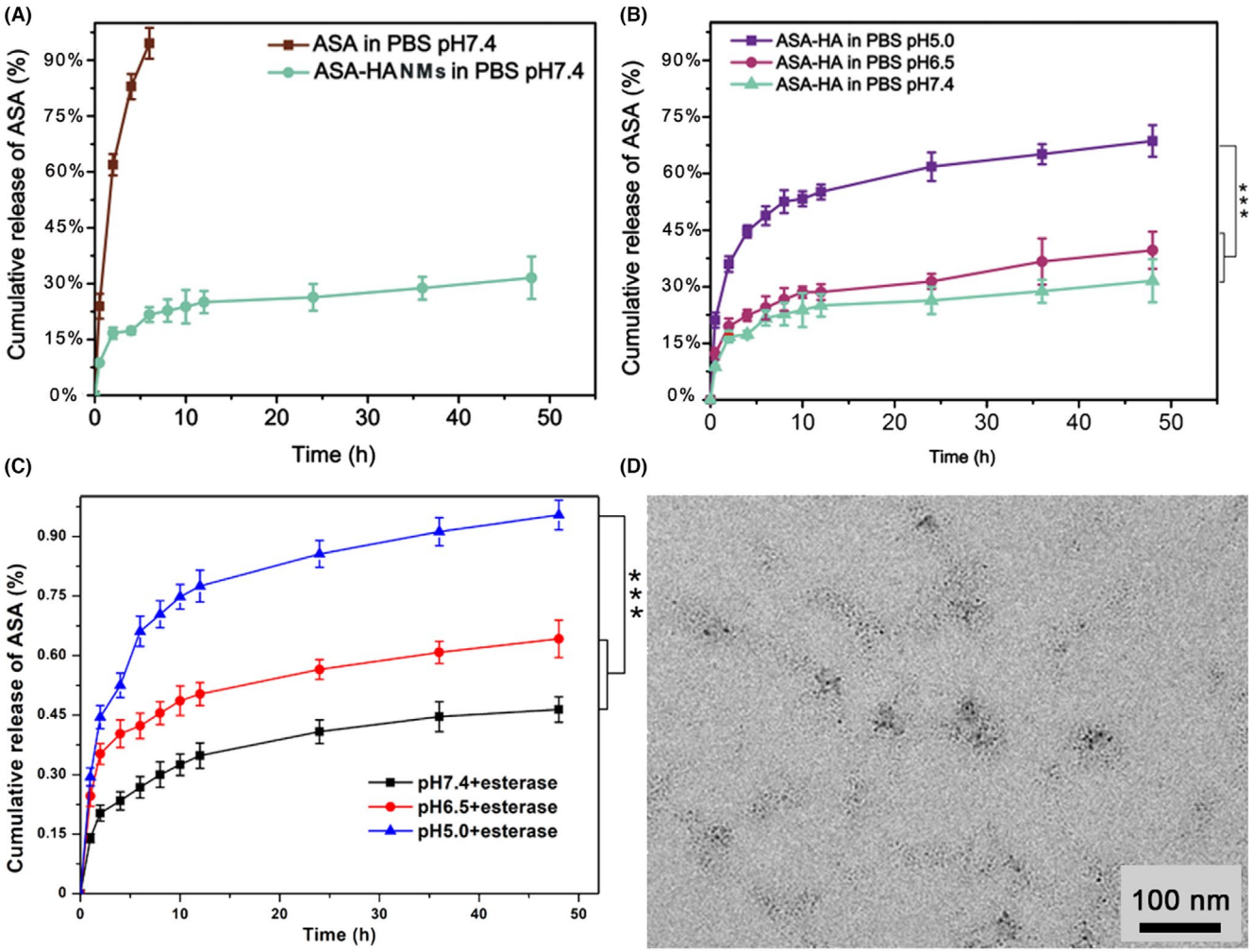

FIGURE 2 In vitro disassembly and drug release of ASA–HA (artesunate–hyaluronic acid) NMs (nanomicelles). (A) In vitro drug release profiles of ASA and ASA–HA NMs at pH 7.4. In vitro drug release profiles of ASA–HA NMs at different pH values (B) without and (C) with esterase (5 mg, 30 U/mL). (D) Transmission electron microscopic image of ASA–HA NMs at pH 5.0 with esterase. All data are represented as mean ± SD (standard deviation) ($n = 3$). ***$p < 0.001$.

FIGURE 3 In vitro cellular uptake and ROS (reactive oxygen species) production. Confocal laser scanning microscopic images (scale bar = 75 μm) of (A) HeLa and (B) A549 cells incubated with ASA^{NBD}–HA NMs (nanomicelles) with/without HA pretreatment for 1 and 4 h (scale bar = 75 μm). (C) Flow cytometry of HeLa treated with ASA^{NBD}, ASA^{NBD} with HA pretreatment, and ASA^{NBD}–HA NMs. (D) Mean fluorescence intensity of ASA^{NBD} and ASA^{NBD}–HA NMs without/with HA pretreatment for 4 h. (E) Confocal laser scanning microscopic images (scale bar = 75 μm) of HeLa, A549, and L02 cells treated with ASA^{NBD} and ASA^{NBD}–HA NMs for 1 and 4 h, respectively. (F) Confocal laser scanning microscopic images of DCFH-stained HeLa cells after incubation for 1 and 4 h with ASA and ASA–HA NMs, respectively (scale bar = 75 μm). All data are represented as mean ± SD (standard deviation) ($n = 3$). **$p < 0.01$.

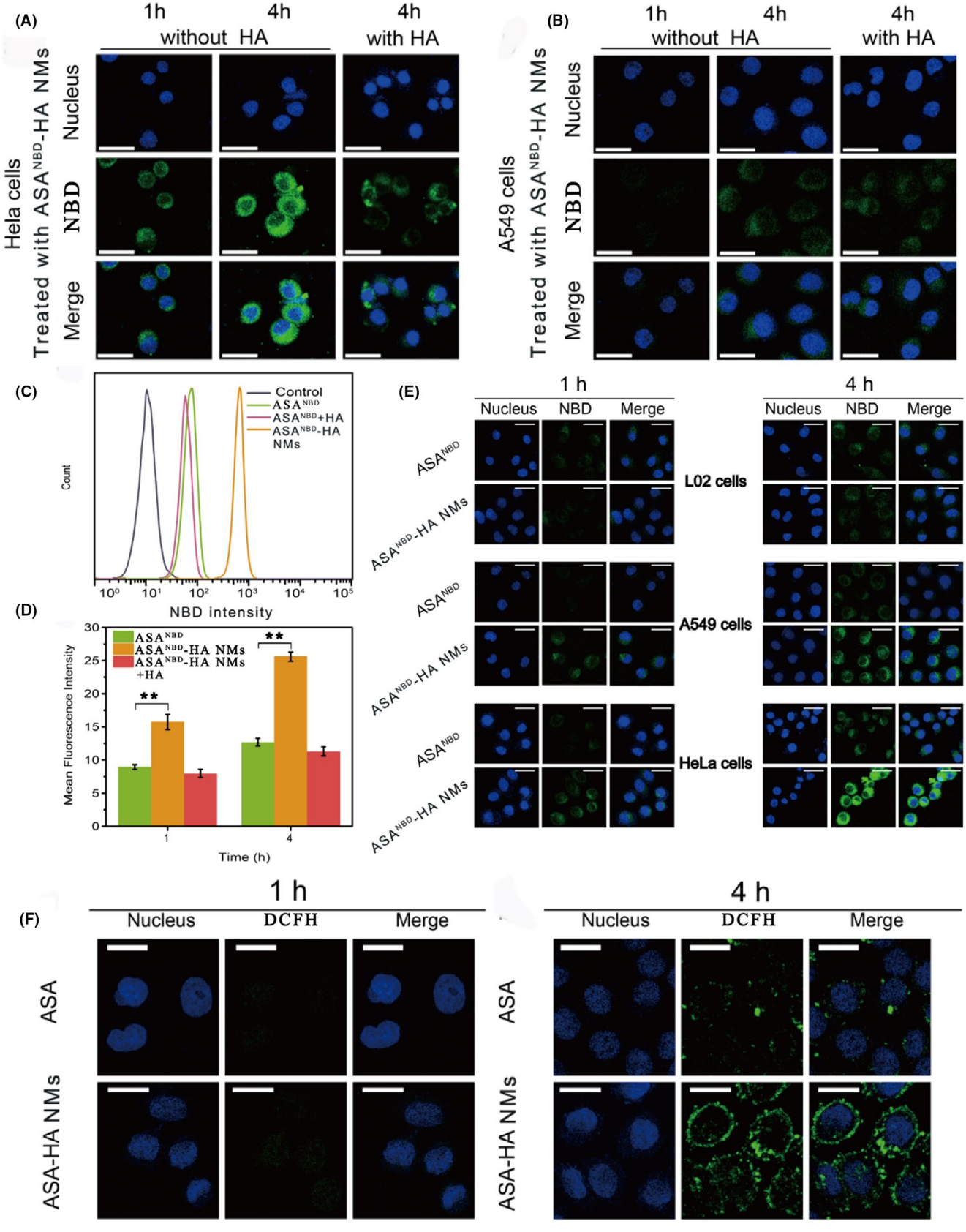

When the tumor volume became ~150 mm^3, 200 μL of $ASA^{Cy5.5}$ and $ASA^{Cy5.5}$–HA NMs based on 0.4 mg/kg of Cy5.5 concentration was intravenously injected into the 4T1 tumor-bearing mice through the tail vein. After intravenous injection at 1, 2, 4, 8, 12, and 24 h, in vivo fluorescence images were captured using the Small Animal Live Fluorescence Imaging System FX pro (Carastream, USA) and

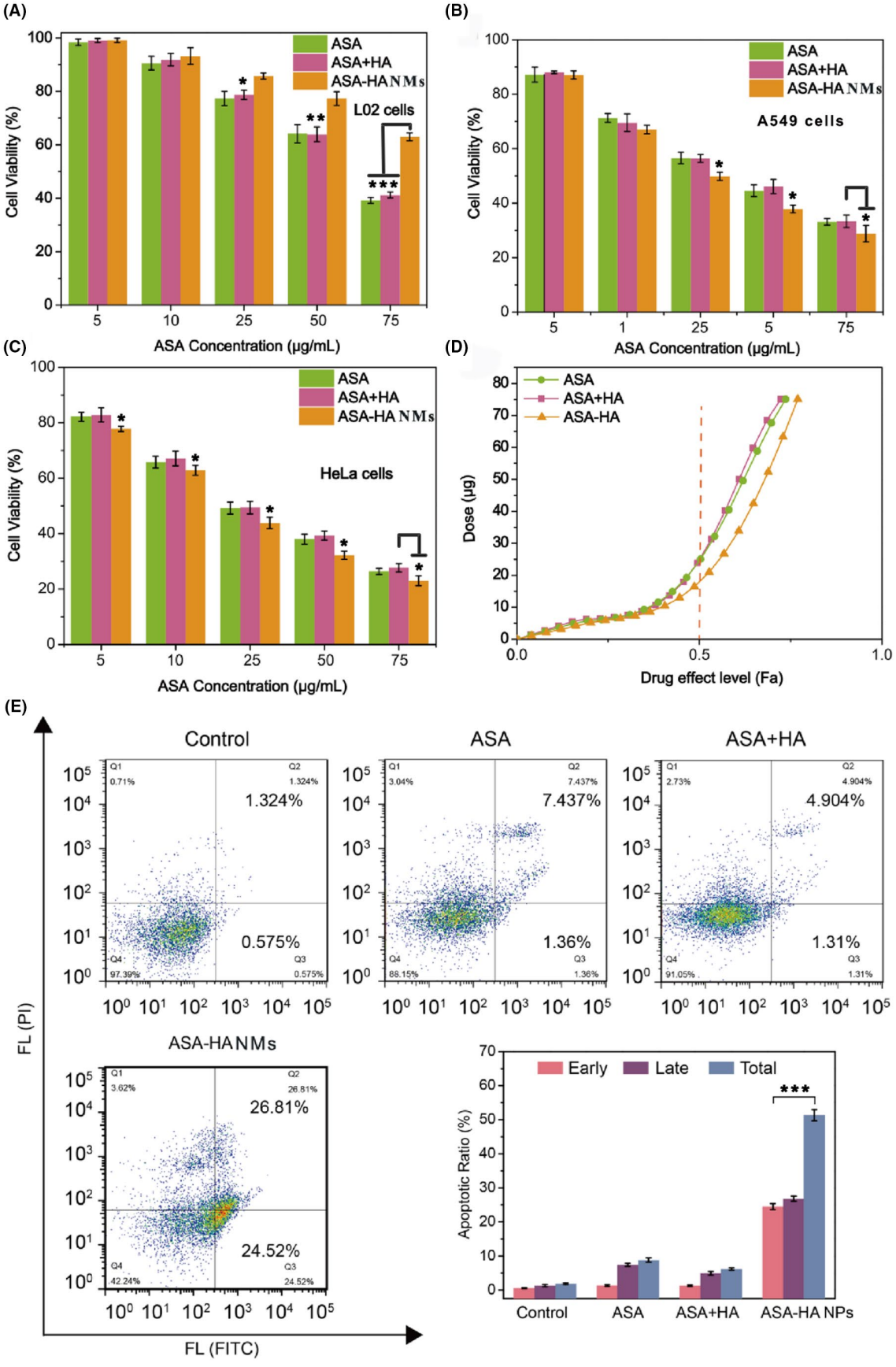
(A)
Cell Viability (%)
ASA
ASA+HA
ASA-HA NMs
L02 cells
ASA Concentration (μg/mL)
(B)
Cell Viability (%)
ASA
ASA+HA
ASA-HA NMs
A549 cells
ASA Concentration (μg/mL)
(C)
Cell Viability (%)
ASA
ASA+HA
ASA-HA NMs
HeLa cells
ASA Concentration (μg/mL)
(D)
Dose (μg)
ASA
ASA+HA
ASA-HA
Drug effect level (Fa)
(E)
Control
ASA
ASA+HA
ASA-HA NMs
1.324%
0.575%
7.437%
1.36%
4.904%
1.31%
26.81%
24.52%
FL (PI)
FL (FITC)
Early
Late
Total
Apoptotic Ratio (%)
Control
ASA
ASA+HA
ASA-HA NPs

FIGURE 4 In vitro antitumor evaluation of ASA–HA (artesunate–hyaluronic acid) NMs (nanomicelles). Cell viability of (A) L02, (B) A549, and (C) HeLa cells incubated with ASA, ASA + HA, and ASA–HA NMs at different concentration gradients for 24 h. (D) IC_{50} (half-maximal inhibitory concentration) value of ASA, ASA + HA, and ASA–HA NMs. (E) Apoptosis of HeLa cells incubated with ASA, ASA + HA, and ASA–HA NMs for 24 h. All data are represented as mean ± SD (standard deviation) ($n = 3$). $^{*}p < 0.05$, $^{**}p < 0.01$, and $^{***}p < 0.001$.

subsequently semiquantitatively analyzed using the Living Image Software.

After a 24-h intravenous injection, the tumor-bearing mice were euthanized. Major organs and tumors were obtained, and ex vivo fluorescence images were acquired utilizing the Small Animal Live Fluorescence Imaging System FX pro (Carastream). Semi-quantitative analysis was then carried out using the Living Image software.

2.12 | In vivo antitumor effect

In vivo antitumor effect of ASA–HA NMs was assessed in tumor-bearing mice. Once the tumor volume reached ~150 mm^3, the 4T1 tumor-bearing mice were randomly divided into three groups. Then, the tumor size of every mouse was determined using a caliper every 2 days for 21 days. After the 21-day therapy period, all mice were humanely euthanized. Subsequently, the subcutaneous tumors and major organs (heart, liver, spleen, lung, and kidney) were excised, weighed, and rinsed with saline thrice. To assess tissue damage and cell apoptosis post-therapy, the collected tumors and major organs were sectioned into small pieces, fixed in 10% formalin, and embedded in paraffin blocks. The treated tissues embedded in paraffin were then sliced into 8-μm sections, stained with hematoxylin and eosin (H&E), and examined using a light microscope (Nikon Eclipse Ci, Tokyo, Japan).

2.13 | Hemolysis assay

Hemolysis assay was conducted to evaluate the biocompatibility of ASA–HA NMs. Briefly, blood samples from Sprague–Dawley rats' retro-orbital choroid plexus were obtained under mild anesthesia; the red blood cells were isolated by centrifugation and washed thrice with PBS (pH 7.4) until the supernatant turned colorless. Then, 200 μL of cell suspension was diluted to 10% (v/v) of cell suspension. For the experimental groups, 1 mL of HA (1000 μM), ASA (10, 100, and 1000 μM), and ASA–HA NMs (10, 100, and 1000 μM) was injected dropwise into 200 μL of cell suspension separately. Finally, the UV–Vis absorption spectrum of the obtained supernatant at 541 nm was assessed using a UV–Vis. spectrophotometer UV2550 (Shimadzu).

2.14 | Statistical analysis

All data were represented as mean ± standard deviation. Statistical differences among groups were analyzed using one-way analysis of variance (ANOVA) and Tukey's posttest. $p < 0.05$ was considered to be statistically significant ($^{**}p < 0.01$ and $^{***}p < 0.001$).

3 | RESULTS

3.1 | Synthesis and characterization of ASH–HA conjugate

The amphiphilic drug–polymer ASH–HA conjugate was first successfully synthesized through the esterification reaction by dehydration between the carboxyl group of ASA and the hydroxyl group of HA (Figure S1). To further confirm the formation mechanism of the ASA–HA conjugate, UV–Vis. absorbance spectrum, FT-IR spectroscopy, ^{1}H-NMR, and XRD were carried out. Figure 1A shows that the physical mixture (referred to as ASA + HA) of ASA and HA exhibited an absorption peak at 235 nm, attributed to the presence of both ASA and HA. Moreover, a thorough examination revealed that the peak at 235 nm in the ASA–HA conjugate had shifted to 239 nm and exhibited a new characteristic peak at 285 nm. This observation indirectly confirmed the successful synthesis of the ASA–HA conjugate. Additionally, Figure 1B shows a distinct absorption peak at 1744 cm^{-1} in the ASA–HA conjugate, setting it apart from ASA, HA, and ASA + HA. This peak can be attributed to the stretching vibration of the C=O group from the ester bond.[25] In addition, the absorption peak at 1753 cm^{-1}, indicative of the carboxyl group, disappeared in ASA on conjugation with HA. Instead, two specific peaks characteristic of ASA emerged in the ASA–HA conjugate. Similarly, Figure 1C shows the distinctive ^{1}H-NMR spectra of ASA and HA evident in the ASA conjugate. Furthermore, the new characteristic peak at 2.62 ppm was observed in the ASA–HA conjugate, which could be due to the appearance of the proton from the ester bond.[26] These data jointly revealed the appearance of the ester bond between ASA and HA to form the ASA–HA conjugate.

Next, to further explore the crystal structure of the ASA–HA conjugate, the XRD experiment was also conducted. Figure 1D shows that ASA exhibited obvious crystal diffraction peaks because of the crystallization properties of ASA. On the contrary, HA exhibited a broad peak, suggesting that HA belonged to an amorphous compound.[27] Remarkably, the XRD spectrum of ASA + HA clearly showed that certain crystalline peaks were still present, indicating that ASA in its crystalline form persisted in the physical mixture. Conversely, all crystalline peaks disappeared in the XRD spectrum of the ASA–HA conjugate, attributed to the formation of the ester bond.[28] Therefore, the aforementioned experimental results jointly verified the successful synthesis of the ASA–HA conjugate.

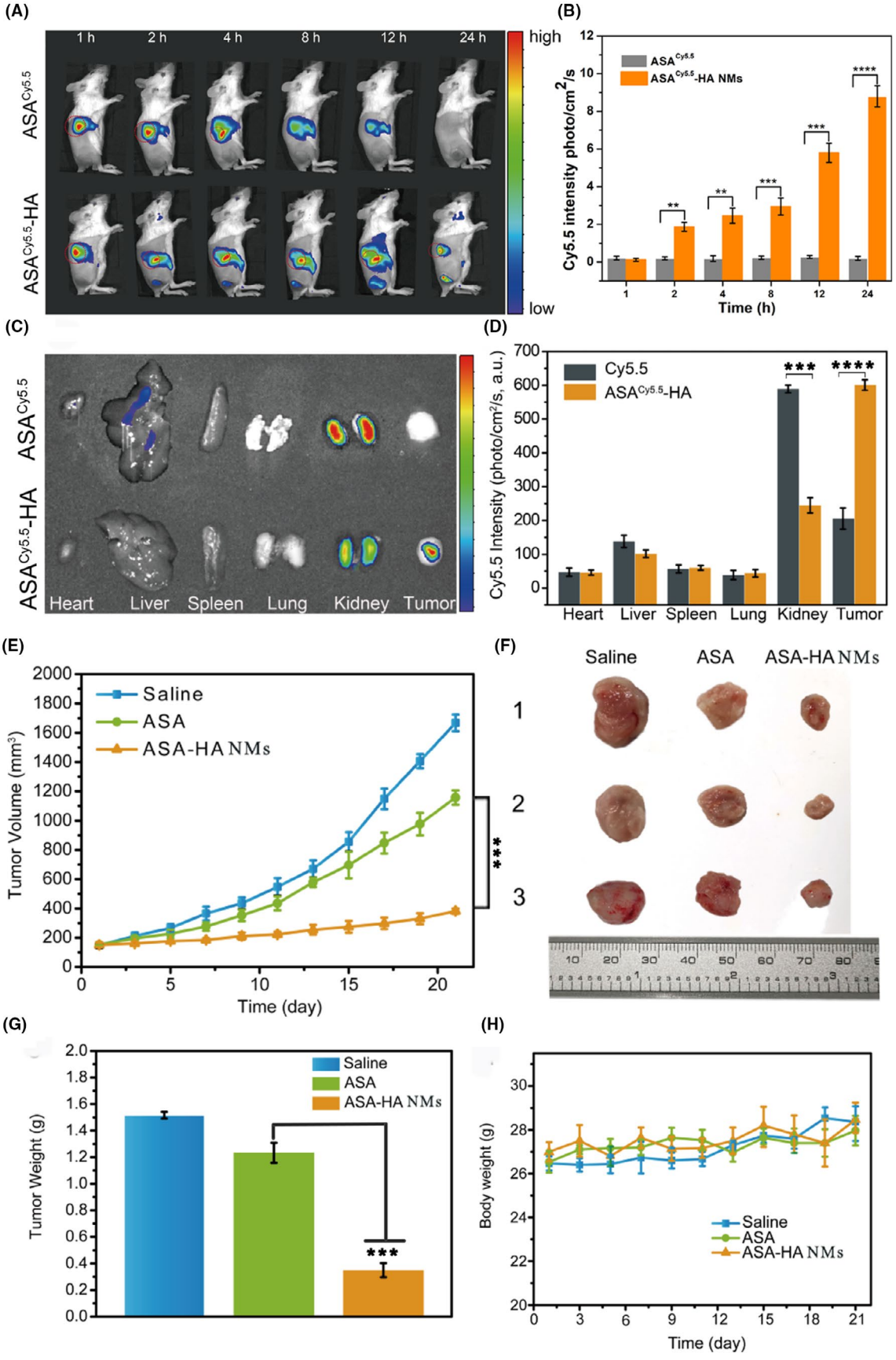
(A)
1 h
2 h
4 h
8 h
12 h
24 h
high
low
ASA^Cy5.5
ASA^Cy5.5-HA
(B)
ASA^Cy5.5
ASA^Cy5.5-HA NMs
Cy5.5 intensity photo/cm^2/s
Time (h)
(C)
Heart
Liver
Spleen
Lung
Kidney
Tumor
(D)
Cy5.5
ASA^Cy5.5-HA
Cy5.5 Intensity (photo/cm²/s, a.u.)
(E)
Saline
ASA
ASA-HA NMs
Tumor Volume (mm³)
Time (day)
(F)
Saline
ASA
ASA-HA NMs
(G)
Tumor Weight (g)
(H)
Body weight (g)
Time (day)

FIGURE 5 In vivo fluorescence imaging and antitumor evaluation of ASA–HA (artesunate–hyaluronic acid) NMs (nanomicelles). (A) Representative in vivo fluorescence images and (B) corresponding semiquantitative analysis of 4T1 tumor-bearing mice after intravenous injection of $ASA^{Cy5.5}$ and $ASA^{Cy5.5}$–HA NMs at equal $ASA^{Cy5.5}$ concentration. (C) Representative ex vivo fluorescence images and (D) corresponding semiquantitative analysis of major organs and tumors from 4T1 tumor-bearing mice after intravenous injection of $ASA^{Cy5.5}$ and $ASA^{Cy5.5}$–HA NMs at equal $ASA^{Cy5.5}$ concentration. Changes in (E) tumor volume of 4T1 tumor-bearing mice treated with saline, ASA, and ASA–HA NMs for 21 days. (F) Images and (G) weight of representative excised tumors after therapy with saline, ASA, and ASA–HA NMs for 21 days. (H) Changes in body weight of 4T1 tumor-bearing mice treated with saline, ASA, and ASA–HA NMs for 21 days. All data are represented as mean ± SD (standard deviation) ($n = 3$). $^{**}p < 0.01$, $^{***}p < 0.001$, and $^{****}p < 0.0001$.

3.2 | Construction and characterization of ASH–HA NMs

The ASA–HA conjugate could readily self-assemble as nanoparticles in an aqueous solution because of its inherent amphiphilic properties.[29] Inspired by this factor, numerous attempts revealed that the ASA–HA conjugate could be synthesized via the cosolvent method. Figure S2 shows that the CMC value of ASA–HA NMs was 27 μg/mL, indicating that the ASA–HA conjugate had a good self-assembly ability to form ASA–HA NMs. Therefore, the average hydrodynamic particle size and zeta potential of ASA–HA NMs were detected using DLS and ELS, respectively. Figure 1E shows that ASA–HA NMs exhibited a uniform hydrodynamic size of ~180 nm and superior dispersibility polydispersity index (PDI = 0.14). Furthermore, Figure 1F shows that the zeta potential of ASA–HA NMs was found to be −23 mV, indicating good stability likely attributed to the presence of ester bonds.[30] Furthermore, Figure 1G,H shows that a regular spherical morphology, uniform diameter, integrated structure, and good dispersion were observed using a transmission electron microscope. The aforementioned results confirmed that ASA–HA NMs have not only been successfully synthesized but also exhibited good physicochemical properties. Simultaneously, Figure S3 shows standard curves constructed for the quantification of subsequent ASA. Furthermore, it is important to highlight that the drug payload of ASA–HA nanoparticles amounted to 30 wt%. Such a high drug payload can be attributed to the fact that HA as a polysaccharide has many hydroxy groups, which can graft with the carboxyl groups of ASA to form the amphiphilic drug–polymer conjugate ASA–HA.

3.3 | pH- and esterase-responsive drug release of ASA–HA NMs

It is widely recognized that the outstanding physiological stability and on-demand drug release of nanodrugs can effectively prevent premature drug leakage or off-target release during blood circulation. Instead, they can be rapidly released at the lesion site using controlled release methods.[31] Therefore, to establish the basis for subsequent in vitro or in vivo experiments, we conducted further evaluations of the physiological stability and the drug release profiles responsive to pH and esterase of ASA–HA nanoparticles.

To assess the physiological stability of ASA–HA nanoparticles, we conducted DLS experiments at different time intervals. Figure S4 shows that the hydrodynamic particle size of ASA–HA nanoparticles did not exhibit significant changes after being incubated with water and PBS for 5 days. This finding suggests that ASA–HA nanoparticles possess excellent physiological stability in a biological medium, indicating their capacity to maintain an intact nanostructure and high stability during blood circulation, which is likely advantageous for tumor accumulation.

The amphiphilic nature of the ASA–HA conjugate, along with the intermolecular interactions among the conjugates, enables the self-assembly of NMs.[32] In addition, the ASA–HA conjugate was linked by a hydrolyzable ester bond. Therefore, it is reasonable to speculate that ASA–HA NMs could disintegrate within the acidic esterase-rich lysosomal environment of tumor cells, leading to the release of ASA. Therefore, the drug release behavior of ASA–HA NMs was evaluated by the simulated physiological condition (pH 7.4) and the acidic medium (pH 5.0) with esterase at 37°C. Figure 2A shows that under neutral conditions and in the absence of esterase, the release of ASA from ASA–HA NMs was less than 30% within 24 h, indicating the excellent stability of ASA–HA under physiological conditions when compared to ASA alone. By contrast, the released quantity of ASA from ASA–HA NMs was more than 60% at pH 5.0 after incubation for 24 h (Figure 2B), indicating that ASA–HA NMs could be partly disassembled in the weakly acidic medium (see Figure S5). Moreover, a distinct contrast was observed, where the presence of esterase noticeably enhanced the release of ASA from ASA–HA NMs. It should be pointed out that the released quantity of ASA from ASA–HA NMs reached at more than 95.4% after incubation for 48 h (Figure 2C), suggesting that ASA–HA NMs could be thoroughly disassembled in the acidic medium (pH 5.0) with esterase (Figure 2D). These experimental findings suggest that ASA–HA NMs have the potential to significantly improve cellular uptake efficiency in tumor cells via CD44 receptor-mediated transcytosis.

3.4 | In vitro cellular uptake and intracellular ROS storm

Based on our hypothesis, the efficient cellular uptake of ASA–HA NMs in tumor cells through CD44 receptor-mediated transcytosis plays a pivotal role in enabling intracellular Fe^{2+} to catalyze the released ASA, resulting in the production of a highly toxic $\bullet O_2^-$ storm that amplifies intracellular oxidative stress. Therefore, to evaluate the cellular uptake effect of ASA–HA NMs using qualitative confocal laser scanning microscopy (CLSM) and quantitative flow cytometry, ASA was labeled with NBD-Cl with a very small molecular structure

by a nucleophilic substitution reaction (termed as ASA^{NBD}). Next, high CD44 receptor expression in HeLa cells, low expression in A549 cells, and no expression in L02 cells were cultured with ASA^{NBD} and ASA^{NBD}–HA NMs for 1 or 4 h. As shown in Figure 3A–C, the fluorescence intensity of NBD demonstrates that ASA^{NBD}–HA NMs exhibited greater internalization in HeLa and A549 cells compared with ASA^{NBD} or ASA^{NBD} + HA at the same time point. In addition, the cellular uptake effect of ASA^{NBD}–HA NMs was obviously enhanced on increasing the incubation time. These experimental results demonstrate that the incorporation of the nanostructure significantly enhanced the cellular uptake efficiency.[33] In addition, observations revealed that HeLa cells preincubated with excessive HA as a CD44 receptor blocker significantly inhibited the cellular uptake of ASA^{NBD}–HA NMs. This result revealed that ASA^{NBD}–HA NMs might specifically recognize HeLa cells by self-targeting CD44 receptors due to the specifically binding affinity of HA ligands on the surface of ASA^{NBD}–HA NMs. To further confirm the aforementioned hypothesis, the selective cellular uptake of ASA^{NBD}–HA NMs was also evaluated using HeLa, A549, and L02 cells. Figure 3E shows that the fluorescence intensity of ASA^{NBD}–HA NMs in HeLa cells was significantly higher compared to that in A549 or L02 cells. Therefore, these experimental results, in conjunction with prior studies, collectively demonstrate that ASA–HA NMs exhibited a selective self-targeting effect. This effect stems from the binding affinity of HA ligands on the surface of ASA–HA NMs to CD44 receptors on the HeLa cell membrane, resulting in efficient cellular uptake of ASA–HA NMs.

After the effectiveness of ASA–HA NMs in selectively targeting tumor cells with CD44 receptors, the intracellular ROS levels were subsequently assessed using the DCFH-DA probe. After diffusion into the cytoplasmic matrix, DCFH-DA could be oxidized into the DCF with fluorescence via ROS. The fluorescence signals of DCFH in HeLa cells were further evaluated using CLSM. Figure 3F shows that after HeLa cells were incubated by ASA and ASA–HA NMs for 1 h, no obvious DCFH fluorescence signals could be found in cells. In contrast, after culture for 4 h, HeLa cells treated with ASA–HA NMs exhibited much stronger fluorescence signals compared with ASA; Figure S6 shows that, simultaneously, the corresponding semiquantitative results confirmed the sharp increase in fluorescence levels at 4 h. These experimental results strongly imply that ASA–HA NMs could produce the highly toxic $\bullet O_2^-$ storm for self-amplifying intracellular oxidative stress, thereby expecting to achieving the highly efficient antitumor.

3.5 | In vitro cytotoxicity of ASA–HA NMs

The highly intracellular ROS level can induce oxidative stress, thereby resulting in irreversible apoptosis.[34] Using the selective cellular uptake and intracellular ROS production of ASA–HA NMs, its potential antitumor effect in vitro was further determined using MTT assay. Figure 4A–C shows that after A549 and L02 cells were treated with ASA, ASA + HA, and ASA–HA NMs for 24 h, no significant difference in cytotoxicity could be found in all groups, which is due to low or no expression of the CD44 receptor on the surface of these cells. Additionally, it is important to highlight that ASA–HA NMs exhibited a clear inhibitory effect on tumor cells with high CD44 receptor expression but almost no toxic effect on normal cells. Moreover, the cytotoxic effect of ASA–HA NMs on HeLa cells was substantially greater than that of ASA and ASA + HA, which is attributed to the enhanced cellular uptake facilitated by the CD44 receptors. The aforementioned experimental results were well consistent with IC_{50} (Figure 4D) and apoptosis (Figure 4E). Consequently, the selective antitumor effect of ASA–HA NMs could be expected to enhance the therapeutic effect and reduce the undesirable side effect.

3.6 | In vivo distribution and antitumor effect

As is well known, the efficient tumor-targeting effect plays a vital role in oncotherapy.[35] In addition, drawing inspiration from the highly selective cellular uptake and antitumor efficacy of ASA–HA NMs in vitro, the self-targeting effect on the solid tumor with the high expression of CD44 receptors was determined using the 4 T1 tumor-bearing mouse model and then evaluated using in vivo fluorescence imaging. Figure 5A,B shows that $ASA^{Cy5.5}$ and $ASA^{Cy5.5}$–HA NMs were distributed in the reticuloendothelial system (RES) system 1 h postinjection. Nevertheless, no $ASA^{Cy5.5}$ was accumulated in the tumor site during the real-time fluorescence imaging period. In addition, $ASA^{Cy5.5}$ almost disappeared 12 h postinjection, which may be attributed to the fact that $ASA^{Cy5.5}$ as a small molecule is subject to entrapment by plasma.[36] As expected, $ASA^{Cy5.5}$–HA NMs could gradually accumulate in tumors over time. To further evaluate the biodistribution of $ASA^{Cy5.5}$–HA NMs, the major organs and tumors were collected 24 h postinjection for ex vivo fluorescence imaging (see Figure 5C,D). In $ASA^{Cy5.5}$–HA NMs, the fluorescence intensity of the tumors was far higher compared with that of other tissues. In addition, an inspection of liver tissues found that the fluorescence intensity of $ASA^{Cy5.5}$ was higher than that of $ASA^{Cy5.5}$–HA NMs, which might be because the hydrophobic $ASA^{Cy5.5}$ were more likely to accumulate in the RES system compared with the amphiphilic $ASA^{Cy5.5}$–HA NMs.[37] Thus, the results of the experiments mentioned earlier provide compelling evidence that ASA–HA NMs could be delivered to the tumor site effectively through the CD44 receptor-mediated self-targeting mechanism.

Motivated by the efficient tumor-targeting effect of ASA–HA NMs, its antitumor effect was further evaluated. In particular, when the tumor volume reached ~150 mm^3, the tumor-bearing mice were randomly assigned to three groups and administered saline (control), ASA, and ASA–HA NMs via tail vein injection every 3 days. Subsequently, the in vivo antitumor efficacy of ASA–HA NMs was assessed. Figure 5E–G shows that on completion of the full treatment cycle the tumor volume in the saline group had increased to nearly 1800 mm^3. Furthermore, there was a partial suppression of tumor volume in the ASA group. In contrast, the ASA–HA NM group

exhibited a notable inhibitory effect on tumor growth. These macroscopic findings were consistent with the microscopic H&E staining of tumor sections (Figure S7). The superior antitumor effect of ASA–HA NMs may be attributed to the fact that ASA–HA NMs can effectively reach the tumor region and be internalized by tumor cells through the CD44 receptor-mediated self-targeting effect. On internalization into tumor cells, the liberated ASA can be catalyzed by endogenous Fe^{2+} within the tumor to produce a highly toxic $\bullet O_2^-$ storm, thus triggering a self-amplifying intracellular oxidative stress response.

3.7 | In vivo biosafety assessment

The assessment of in vivo biosafety plays a crucial role in advancing preclinical drug research.[36,38] Figure S7 shows that the microscopic H&E staining of major organs revealed that ASA–HA NM therapy did not result in obvious histological damages, indicating that it was biosafe for normal tissues. Furthermore, Figure S8 shows that the hemolysis rate was maintained in the normal range (well far below international standards of 5%) after ASA–HA NM therapy, suggesting its good biocompatibility. Thus, the low systemic toxicity of ASA–HA NMs makes it promising for future biomedical applications in clinic.

4 | DISCUSSION

Oxidative stress due to elevated ROS has been extensively studied and proved to play a crucial role in current cancer therapies. ASA exhibited a high ROS yield, which is attributed to the unique peroxo-bridge structure that is broken by endogenous Fe^{2+}, further producing ROS. This study synthesized nanomaterials using esterase- and pH-responsive HA ligands embedded in ASA for specifically targeting cancer cells, releasing ASA on demand and inducing the production of oxidative stress to further amplify the therapeutic effects of ASA.

The synthesis and characterization experiments revealed the changes in the absorption peaks, the formation of new absorption peaks, and the crystal structures of ASA–HA using UV–Vis. absorption spectroscopy, FT-IR spectroscopy, ^{1}H-NMR spectroscopy, and XRD experiments. Overall, these analyses demonstrated the successful formation of ester bonds between ASA and HA, which led to the formation of ASA–HA conjugates. Meanwhile, the CMC proved that the ASA–HA NMs exhibited good self-assembly ability, and the TEM and DLS results showed that the ASA–HA NMs were spherical, uniform in size, structurally intact, and well dispersed. Further response release experiments proved that ASA–HA NMs exhibited pH- and esterase-response release ability, which lays a good basis for subsequent in vitro and in vivo experiments.

Cellular experiments revealed that ASA–HA NMs achieved strong cellular uptake by cancer cells through a CD44 receptor-mediated mechanism, which led to the production of ROS storms. Meanwhile, further evaluation of the killing effect on cancer cells revealed that ASA–HA NMs were able to enhance the anticancer effect and were less lethal to normal cells.

In vivo experiments analyzed the retention and distribution of ASA–HA in tumor-bearing mice using fluorescence imaging, and the results showed that ASA–HA NMs could specifically target tumor tissues and reduce the distribution in other tissues, and the superior anticancer ability of ASA–HA NMs was also confirmed, which may be due to the fact that they can effectively reach the tumor site through the CD44 receptor-mediated mechanism, followed by the responsive release of ASA drug in the presence of pH and esterase, which interrupts the peroxo-bridge bond by endogenous Fe^{2+}, thereby producing a ROS storm and causing oxidative stress-induced cell death.

In conclusion, by combining clinically approved drugs using advanced nanotechnology, our work not only improves the feasibility of clinical translation but also opens up avenues for innovative applications of existing drugs. Therefore, accelerating further research and clinical studies is essential to fully realize the therapeutic potential of these agents and expedite their clinical application.

5 | CONCLUSIONS

Building on the concept of non-Fenton CDT, we successfully designed endogenous Fe^{2+}-triggered self-targeting ASA–HA NMs that are pH- and esterase responsive for self-amplifying intracellular oxidative stress mediated by ROS production. After administration via tail vein injection, these NMs with a high drug payload can efficiently target the tumor site and enter tumor cells through CD44 receptor-mediated transcytosis. Furthermore, our experimental results confirmed that these NMs can disassemble within the acidic esterase-rich lysosomal environment of tumor cells, facilitating the on-demand burst release of ASA. Importantly, the ASA released from ASA–HA NMs, acting as a non-Fenton substrate, can be catalyzed by tumor endogenous Fe^{2+} to produce a highly toxic $\bullet O_2^-$ storm, leading to self-amplifying intracellular oxidative stress. Moreover, both in vitro and in vivo experimental outcomes collectively demonstrated the substantial antitumor efficacy of ASA–HA NMs, which is attributed to the incorporation of the self-targeting concept. In conclusion, the design and development of enhanced formulations utilizing clinically approved drugs have the potential to expedite clinical research, facilitate the commercialization of drugs, strategically innovate new applications for clinically approved medications, and represent a promising avenue for drug discovery.

AUTHOR CONTRIBUTIONS

Zhongxiong Fan: conceptualization, data curation, formal analysis, investigation, methodology, project administration, software, validation, visualization, and writing—original draft; Guoyu Xia: conceptualization, data curation, formal analysis, investigation,

methodology, project administration, software, validation, visualization, and writing—original draft; Qingluo Wang: data curation, formal analysis, investigation, software, validation, and visualization; Shiduan Chen: formal analysis, investigation, software, validation, and visualization; Jianmin Li: formal analysis, investigation, software, validation, and visualization; Zhenqing Hou: formal analysis, investigation, validation, and visualization; Ziwen Jiang: funding acquisition, formal analysis, investigation, validation, and visualization; Juan Feng: conceptualization, funding acquisition, investigation, methodology, project administration, resources, software, supervision, validation, visualization, writing—original draft, and writing—review and editing.

ACKNOWLEDGEMENT

Zhongxiong Fan greatly thanks Heng Sun at Xi'an Jiaotong University and Dao Shi at Shanghai Jiao Tong University.

FUNDING INFORMATION

We acknowledge the financial support from the National Natural Science Foundation of China (82000152), Key Research and Development Program in Xinjiang Uygur Autonomous Region (2023B02030 and 2023B02030-1), Autonomous Region Universities Basic Research Funds Research Projects-Cultivation Projects (XJEDU2023P017), Natural Science Foundation of Xinjiang Uygur Autonomous Region (2022D01C698), and the Xinjiang Uygur Autonomous Region Tianchi Talent Introduction Program-Young Doctor (51052300514).

CONFLICT OF INTEREST STATEMENT

The authors declare that they have no known competing financial interests or personal relationships that could have appeared to influence the work reported in this paper.

ETHICS STATEMENT

All animal experiments were carried out based on a protocol approved via the Institutional Animal Care and Use Committee of Xiamen University.

ORCID

Zhongxiong Fan https://orcid.org/0000-0001-5751-9530
Zhenqing Hou https://orcid.org/0000-0002-5537-075X

REFERENCES

1. Wang Z, Zhang Y, Ju E, et al. Biomimetic nanoflowers by self-assembly of nanozymes to induce intracellular oxidative damage against hypoxic tumors. *Nat Commun*. 2018;9(1):3334.
2. Wu Y, Li Y, Lv G, Bu W. Redox dyshomeostasis strategy for tumor therapy based on nanomaterials chemistry. *Chem Sci*. 2022;13(8):2202-2217.
3. Yu X, Zhang Y-C, Yang X, et al. Bonsai-inspired AIE nanohybrid photosensitizer based on vermiculite nanosheets for ferroptosis-assisted oxygen self-sufficient photodynamic cancer therapy. *Nano Today*. 2022;44:101477.
4. Liang S, Yao J, Liu D, Rao L, Chen X, Wang Z. Harnessing nanomaterials for cancer sonodynamic immunotherapy. *Adv Mater*. 2023;35(33):2211130.
5. Du Z, Wang X, Zhang X, et al. X-ray-triggered carbon monoxide and manganese dioxide generation based on scintillating nanoparticles for cascade cancer radiosensitization. *Angew Chem Int Ed*. 2023;62(23):e202302525.
6. Xie W, Guo Z, Zhao L, Wei Y. The copper age in cancer treatment: from copper metabolism to cuproptosis. *Prog Mater Sci*. 2023;138:101145.
7. Pan P, Dong X, Chen Y, Ye J-J, Sun Y-X, Zhang X-Z. A heterogenic membrane-based biomimetic hybrid nanoplatform for combining radiotherapy and immunotherapy against breast cancer. *Biomaterials*. 2022;289:121810.
8. Li Y, Zhao P, Gong T, et al. Redox dyshomeostasis strategy for hypoxic tumor therapy based on DNAzyme-loaded electrophilic ZIFs. *Angew Chem Int Ed*. 2020;59(50):22537-22543.
9. Li X, Zhou Q, Japir AA-WMM, Dutta D, Lu N, Ge Z. Protein-delivering nanocomplexes with Fenton reaction-triggered cargo release to boost cancer immunotherapy. *ACS Nano*. 2022;16(9):14982-14999.
10. Li Q, Yu J, Lin L, et al. One-pot rapid synthesis of Cu^{2+}-doped GOD@MOF to amplify the antitumor efficacy of chemodynamic therapy. *ACS Appl Mater Interfaces*. 2023;15(13):16482-16491.
11. Xiang S, Fan Z, Ye Z, et al. Endogenous Fe^{2+}–activated ROS nanoamplifier for esterase-responsive and photoacoustic imaging-monitored therapeutic improvement. *Nano Res*. 2022;15(2):907-918.
12. Wang S, Yu K, Yu Z, et al. Targeting self-enhanced ROS-responsive artesunatum prodrug nanoassembly potentiates gemcitabine activity by down-regulating CDA expression in cervical cancer. *Chin Chem Lett*. 2023;34(7):108184.
13. Fan Z, Jiang B, Zhu Q, et al. Tumor-specific endogenous FeII-activated, MRI-guided self-targeting gadolinium-coordinated theranostic nanoplatforms for amplification of ROS and enhanced chemodynamic chemotherapy. *ACS Appl Mater Interfaces*. 2020;12(13):14884-14904.
14. Ismail M, Yang W, Li Y, et al. Targeted liposomes for combined delivery of artesunate and temozolomide to resistant glioblastoma. *Biomaterials*. 2022;287:121608.
15. Wang D, He IW, Liu J, et al. Missing-linker-assisted artesunate delivery by metal–organic frameworks for synergistic cancer treatment. *Angew Chem Int Ed*. 2021;60(50):26254-26259.
16. Gao Y, Zhang H, Tang L, et al. Cancer nanobombs delivering artoxplatin with a polyigniter bearing hydrophobic ferrocene units upregulate PD-L1 expression and stimulate stronger anticancer immunity. *Adv Sci*. 2024;11:e2300806.
17. Xiao X, Wang Y, Chen J, et al. Self-targeting platinum(IV) amphiphilic prodrug nano-assembly as radiosensitizer for synergistic and safe chemoradiotherapy of hepatocellular carcinoma. *Biomaterials*. 2022;289:121793.
18. Fan Z, Shi D, Zuo W, et al. Trojan-horse diameter-reducible nanotheranostics for macroscopic/microscopic imaging-monitored chemo-antiangiogenic therapy. *ACS Appl Mater Interfaces*. 2022;14(4):5033-5052.
19. Bhattacharyya M, Jariyal H, Srivastava A. Hyaluronic acid: more than a carrier, having an overpowering extracellular and intracellular impact on cancer. *Carbohydr Polym*. 2023;317:121081.
20. Ming J, Zhu T, Yang W, et al. Pd@Pt-GOx/HA as a novel enzymatic cascade nanoreactor for high-efficiency starving-enhanced chemodynamic cancer therapy. *ACS Appl Mater Interfaces*. 2020;12(46):51249-51262.
21. Nakka K, Hachmer S, Mokhtari Z, et al. JMJD3 activated hyaluronan synthesis drives muscle regeneration in an inflammatory environment. *Science*. 2022;377(6606):666-669.
22. Liu J, Smith S, Wang C. Photothermal attenuation of cancer cell stemness, chemoresistance, and migration using CD44-targeted MoS2 nanosheets. *Nano Lett*. 2023;23(5):1989-1999.

23. Fan Z, Jiang B, Shi D, et al. Selective antitumor activity of drug-free TPGS nanomicelles with ROS-induced mitochondrial cell death. *Int J Pharm*. 2021;594:120184.
24. Fan Z, Jin H, Tan X, et al. ROS-responsive hierarchical targeting vehicle-free nanodrugs for three-pronged Parkinson's disease therapy. *Chem Eng J*. 2023;466:143245.
25. Huang P, Wang D, Su Y, et al. Combination of small molecule prodrug and nanodrug delivery: amphiphilic drug–drug conjugate for cancer therapy. *J Am Chem Soc*. 2014;136(33):11748-11756.
26. Xia X, Yang X, Huang P, Yan D. ROS-responsive nanoparticles formed from RGD–epothilone B conjugate for targeted cancer therapy. *ACS Appl Mater Interfaces*. 2020;12(16):18301-18308.
27. Li Y, Zhang H, Chen Y, et al. Integration of phospholipid-hyaluronic acid-methotrexate nanocarrier assembly and amphiphilic drug–drug conjugate for synergistic targeted delivery and combinational tumor therapy. *Biomater Sci*. 2018;6(7):1818-1833.
28. Fan Z, Wang Y, Xiang S, et al. Dual-self-recognizing, stimulus-responsive and carrier-free methotrexate–mannose conjugate nanoparticles with highly synergistic chemotherapeutic effects. *J Mater Chem B*. 2020;8(9):1922-1934.
29. Fan W, Xiang J, Wei Q, et al. Role of micelle size in cell transcytosis-based tumor extravasation, infiltration, and treatment efficacy. *Nano Lett*. 2023;23(9):3904-3912.
30. Ding Y, Hu X, Piao Y, et al. Lipid prodrug nanoassemblies via dynamic covalent Boronates. *ACS Nano*. 2023;17(7):6601-6614.
31. Wu Q, Hu Y, Yu B, Hu H, Xu F-J. Polysaccharide-based tumor microenvironment-responsive drug delivery systems for cancer therapy. *J Control Release*. 2023;362:19-43.
32. Huang L, Zhao S, Fang F, Xu T, Lan M, Zhang J. Advances and perspectives in carrier-free nanodrugs for cancer chemo-monotherapy and combination therapy. *Biomaterials*. 2021;268:120557.
33. Behzadi S, Serpooshan V, Tao W, et al. Cellular uptake of nanoparticles: journey inside the cell. *Chem Soc Rev*. 2017;46(14):4218-4244.
34. Zhang H, Chen W, Wang J, et al. A novel ROS-activable self-immolative prodrug for tumor-specific amplification of oxidative stress and enhancing chemotherapy of mitoxantrone. *Biomaterials*. 2023;293:121954.
35. Xu Y, Liu R, Li R, et al. Manipulating neovasculature-targeting capability of biomimetic nanodiscs for synergistic photoactivatable tumor infarction and chemotherapy. *ACS Nano*. 2023;17(16):16192-16203.
36. Shi D, Wu F, Huang L, et al. Bioengineered nanogenerator with sustainable reactive oxygen species storm for self-reinforcing sono-chemodynamic oncotherapy. *J Colloid Interface Sci*. 2023;646:649-662.
37. Wang S, Shi H, Wang L, et al. Photostable small-molecule NIR-II fluorescent scaffolds that cross the blood–brain barrier for noninvasive brain imaging. *J Am Chem Soc*. 2022;144(51):23668-23676.
38. Singh N, Kim J, Kim J, et al. Covalent organic framework nanomedicines: biocompatibility for advanced nanocarriers and cancer theranostics applications. *Bioact Mater*. 2023;21:358-380.

SUPPORTING INFORMATION

Additional supporting information can be found online in the Supporting Information section at the end of this article.

How to cite this article: Fan Z, Xia G, Wang Q, et al. Endogenous Fe^{2+}-triggered self-targeting nanomicelles for self-amplifying intracellular oxidative stress. *Anim Models Exp Med*. 2025;8:307-321. doi:10.1002/ame2.12468